This manuscript was accepted by J. Appl. Phys. Click here to see the version of record.

Optical characterization and bandgap engineering of flat and wrinkle-textured $FA_{0.83}Cs_{0.17}Pb(I_{1-x}Br_x)_3$ perovskite thin films

A. Tejada,[1,2,a)] S. Braunger,[2] L. Korte,[2,b)] S. Albrecht,[3] B. Rech,[2] and J. A. Guerra[1,2,c)]

[1)] *Departamento de Ciencias, Sección Física, Pontificia Universidad Católica del Perú, Av. Universitaria 1801, Lima 32, Peru.*

[2)] *Helmholtz-Zentrum Berlin für Materialien und Energie GmbH, Institut für Silizium-Photovoltaik, Kekuléstraβe 5, 12489 Berlin, Germany.*

[3)] *Helmholtz-Zentrum Berlin für Materialien und Energie GmbH, Young Investigator Group for Perovskite Tandem Solar Cells, Kekuléstraβe 5, 12489 Berlin, Germany.*

(Dated: March 26, 2018)

The complex refractive indices of formamidinium cesium lead mixed-halide ($FA_{0.83}Cs_{0.17}Pb(I_{1-x}Br_x)_3$) perovskite thin films of compositions ranging from $x = 0$ to 0.4, with both flat and wrinkle-textured surface topographies, are reported. Films are characterized using a combination of variable angle spectroscopic ellipsometry and spectral transmittance in the wavelength range of 190 nm to 850 nm. Optical constants, film thicknesses and roughness layers are obtained point-by-point by minimizing a global error function, without using optical dispersion models, and including topographical information supplied by a laser confocal microscope. To evaluate the bandgap engineering potential of the material, the optical bandgaps and Urbach energies are then accurately determined by applying a band fluctuations model for direct semiconductors, which considers both the Urbach tail and the fundamental band-to-band absorption region in a single equation. With this information, the composition yielding the optimum bandgap of 1.75 eV for a Si-perovskite tandem solar cell is determined.

I. INTRODUCTION

Organic-inorganic hybrid perovskite materials are currently one of the most promising materials for next generation solar cells[1–10] and other optoelectronic devices,[3,4] owing to their high cell efficiencies, high absorption, direct bandgap, long carrier diffusion length, bandgap tunability and low manufacturing costs.[1–7,10] The use of cesium mixed-cation lead mixed-halide perovskites ($FA_{1-y}Cs_yPb(I_{1-x}Br_x)_3$) has also significantly improved upon the stability issues of classical PV perovskites like $MAPbI_3$.[1,7,10] As such they hold great potential for single junction cells and especially for dual junction Si-perovskite tandem cells. Si solar cells are already approaching the 29% Shockley-Queisser efficiency limit (with the current record at 26.6%[11]), and adding an extra perovskite top cell can potentially increase efficiencies beyond 30% if tuned to the optimal 1.75 eV bandgap.[1–3,12]

Therefore, accurate knowledge of the relation of the complex refractive index $\tilde{n}$, optical bandgap and Urbach energy, to perovskite composition is of great importance. To date, most relevant studies on cesium mixed-cation lead mixed-halide perovskites estimate the bandgap from photoluminescence (PL) measurements,[10] or from direct bandgap fits on an estimation of the absorption coefficient.[1] Also, studies of the complex refractive index obtain $\tilde{n}$ by fitting dispersion models to optical data,[7] which can lead to unwanted artifacts and biases in the results.[5]

In this work, the bandgap engineering potential of two types of $FA_{0.83}Cs_{0.17}Pb(I_{1-x}Br_x)_3$ perovskite films is studied. One presents a flat though somewhat uneven surface topography, which appears to be typical for films of this this type of perovskite manufactured by spin coating. The other presents an unusual, strongly wrinkled self-texturing effect, that produces very optically diffuse films. These may have significant potential for light trapping schemes that can use the perovskite films as grown and on flat substrates suitable for low-cost spin coating processes, without requiring further processing of the layers to achieve sufficient light scattering inside the cell.

For both surface topographies, the complex refractive indices are determined in the wavelength range of 190 nm to 850 nm. This is achieved using a combination of spectral transmittance (T) and variable angle spectroscopic ellipsometry (VASE), which allows the calculation of the absorption coefficient in a wider dynamic range than would be possible with ellipsometry only.[13] The solution algorithm minimizes an error function on a point-by-point basis, i.e. for each measured wavelength, to achieve a self consistent calculation of the complex refractive index, film thickness and root mean square (rms) roughness layer thickness, without using dispersion models. The proposed optical models account for film thickness variation, film surface roughness and internal reflections in the substrate. The optical bandgaps and Urbach energies are subsequently determined using a band fluctuations model for the absorption coefficient of direct semiconductors, which describes both the fundamental band-to-band absorption region and the Urbach tail in a single equation.[5] From these results, the composition for the ideal bandgap of 1.75 eV for Si-perovskite tandem cells is determined.

[a)] Electronic mail: atejadae@pucp.edu.pe
[b)] Electronic mail: korte@helmholtz-berlin.de
[c)] Electronic mail: guerra.jorgea@pucp.edu.pe

II. EXPERIMENTAL DETAILS

A. Perovskite fabrication

Chemicals were purchased from TCI (lead(II) iodide 99.99% Pb, lead(II) bromide 99.99% Pb), Sigma-Aldrich (anhydrous chlorobenzene, anhydrous dimethyl sulfoxide, anhydrous dimethylformamide), ABCR (cesium iodide 99.999% Cs) and Dyenamo (formamidinium iodide 98%), and were used as received.

The $FA_{0.83}Cs_{0.17}Pb(I_xBr_{1-x})_3$ perovskite films were grown on two side polished 500 μm thick fused quartz substrates (for optical measurements) as well as ordinary glass slides (for topography measurements). In both cases, the substrates were consecutively cleaned in acetone, detergent (Mucasol 2 vol% in water), water and isopropanol in an ultrasonic bath for 15 min, respectively. Before layer deposition the substrates were dried in a N_2 stream and treated in an UV ozone cleaner (FHR Anlagenbau GmbH, UVOH 150 LAB) for 15 min.

The perovskite layers were fabricated in a glove box with an N_2 atmosphere in close analogy to previously reported procedures for these compositions.[3,10] The precursor solutions for the various perovskite compositions were obtained by mixing two 1.0M perovskite stock solutions (see Table I) in appropriate ratios (see Table II). The perovskite stock solutions were prepared by weighing the respective solid starting materials into a 5.0 mL volumetric flask and brought up to volume with dimethylformamide and dimethyl sulfoxide (4:1 volume ratio). The precursor solutions were shaken at 60 °C for 30 min and left to cool down to room temperature before blending.

	$FA_{0.83}Cs_{0.17}PbI_3$ **(1)**	$FA_{0.83}Cs_{0.17}Pb(I_{0.60}Br_{0.40})_3$ **(2)**
CsI	221 mg, 0.85 mmol	221 mg, 0.85 mmol
FAI	714 mg, 4.15 mmol	714 mg, 4.14 mmol
$PbBr_2$	-	1.10 g, 3.00 mmol
PbI_2	2.31 g, 5.00 mmol	922 mg, 2.00 mmol
DMF/ DMSO (4:1)	Approx. 4.33 mL (brought to 5.0 mL volume including solids)	

Table I. Quantity of starting materials to obtain perovskite stock solutions **1** and **2** with 1.0M concentration.

Perovskite composition	**Stock solutions (ratio)**
$FA_{0.83}Cs_{0.17}PbI_3$	**1**
$FA_{0.83}Cs_{0.17}Pb(I_{0.90}Br_{0.10})_3$	**1** & **2** (3:1)
$FA_{0.83}Cs_{0.17}Pb(I_{0.80}Br_{0.20})_3$	**1** & **2** (1:1)
$FA_{0.83}Cs_{0.17}Pb(I_{0.70}Br_{0.30})_3$	**1** & **2** (1:3)
$FA_{0.83}Cs_{0.17}Pb(I_{0.60}Br_{0.40})_3$	**2**

Table II. Mixing ratios of stock solutions **1** and **2** to generate the final perovskite precursor solutions used for layer fabrication.

Two deposition procedures were used to yield perovskite layers with flat topographies (Procedure 1, **P1**) and wrinkled topographies (Procedure 2, **P2**). **P1**: Perovskite precursor solution (100 μL) was spread on the substrate and spun in a single step process with open spin coater lid, 4000 rpm for 30 s with an acceleration time of 1 s; during this process chlorobenzene (150 μL) was dripped from 1 cm distance on the center of the spinning substrate after 25 s. The perovskite layer was directly transferred onto a hot plate for annealing at 100 °C for 20 min. **P2**: Perovskite precursor solution (100 μL) was spread on the substrate and spun in a two step process with closed spin coater lid, 1000 rpm for 10 s with an acceleration time of 1 s followed by 6000 rpm for 30 s with an acceleration time of 3 s; during this process chlorobenzene (150 μL) was dripped from 1 cm distance on the center of the spinning substrate after 42 s. The perovskite layer was directly transferred onto a hot plate for annealing at 50 °C for 1 min, then on a second hot plate at 100 °C for 20 min.

B. Optical measurements

Total spectral transmittance was measured with a Perkin Elmer Lambda 1050 UV/VIS/NIR spectrophotometer with an integrating sphere from 250 nm to 1500 nm (5 nm step). The VASE curves were measured with a Sentech SE 850 ellipsometer from 190 nm to 850 nm (∼1 nm step), with incidence angles from 20° to 70°, in 10° increments. The flat film samples were measured with the probing beam incident on the film side, while the wrinkle-textured samples were measured through the backside of the quartz substrate. This was due to the optically diffuse nature of the wrinkle-textured films, which often impeded the ellipsometer from collecting enough light for proper measurements. Because the latter are significantly depolarizing measurements, the degree of polarization was also measured.

Film topography was measured using a Keyence VK-X260 confocal 3D laser scanning microscope with a 408 nm laser at 50x magnification. Care was taken to measure the glass-deposited films in locations similar to those used in the quartz-deposited ones for the transmittance and ellipsometry measurements.

To prevent film degradation, all samples were sealed in plastic bags inside the N_2 atmosphere of the glove box and only removed just before measuring. Degradation during the measurements themselves was considered negligible, as no significant change in the ellipsometry curves was observed during the span of a measurement session.

III. OPTICAL ANALYSIS

A. Extraction of the complex refractive index

The complex refractive index $\tilde{n} = n - ik$, where n is the refractive index and k is the extinction coefficient, is obtained using a combination of spectral transmittance and ellipsometry. This approach is chosen due to the complementary nature of the two techniques: T obtains plenty of information from the bulk of the probed film and is thus very sensitive to the low absorption coefficients found in the fundamental absorption and trans-

parent regions. However, as absorption increases, transmittance approaches zero and no further information can be obtained. Here, ellipsometry can be exploited as it is a very surface sensitive technique which obtains most of its information from the top layer of the film, and is therefore suitable for studying highly absorbing regions.[13] The use of two different techniques also adds more equations to the system, further constraining the final solutions for n and k.[5,6]

The most common strategy for extracting optical constants is to fit curves generated with a dispersion model for $\tilde{n}$ to the experimental data.[4,6,7,13] This has the advantages of being quick and yielding convenient equations for n and k. However, some insight into the fundamental properties of the sample is necessary to select the appropriate dispersion model, and there are many to choose from.[13] If the model is inadequate, it can be unclear whether certain features in $\tilde{n}$ are genuine or if they are artifacts caused by forcing an incorrect model.[5] For lead halide perovskites in particular, the Forouhi-Bloomer,[4,6] Tauc-Lorentz[4,7] and Drude-Lorentz[4] dispersions have been used.

The approach used in this work instead is to self consistently determine $\tilde{n}$ for each individual wavelength, i.e. 'point-by-point'. This is done by numerically solving a system of equations of the type shown in Eq. (1).

$$M_{i,j}^{\mathrm{exp}} - M_j^{\mathrm{th}}\left(n_i, k_i, \lambda_i\right) = 0 \tag{1}$$

Here, $M_{i,j}^{\mathrm{exp}}$ is a vector containing entries representing experimental optical data (in this case, T and/or VASE) at the wavelength λ_i, and $M_j^{\mathrm{th}}\left(n_i, k_i, \lambda_i\right)$ is the theoretical value for $M_{i,j}^{\mathrm{exp}}$ as a function of λ_i, as well as of discrete values for n and k chosen by the solution algorithm. The index j runs through the independent measurement sets, e.g. T, ψ, Δ. Assuming the film thickness and other such parameters are known, in principle only two measurement sets should suffice to obtain $n\left(\lambda\right)$ and $k\left(\lambda\right)$. In practice, this typically yields noisy solution curves with several artifacts,[5] such as diverging solution branches,[14] discontinuities and non-physical values. The reasons for this are two-fold: first, the solution process is highly sensitive to measurement noise, as M_j^{th} is usually very strongly dependent on n_i and k_i, such that small variations in $M_{i,j}^{\mathrm{exp}}$ yield comparatively large variations in n_i and k_i. Second, when solved numerically, a system of only two equations such as this one often allows several possible values for the algorithm to converge to.

To mitigate the aforementioned issues, redundancy is increased by adding more measurement sets for the same sample. In this work, this is done by adding ellipsometry data obtained for several angles. Doing so averages out the effect of measurement noise and constrains the number of possible solution curves for n and k. Similar results have also been achieved using multi-sample analyses.[8,9]

B. Solution algorithm

The self consistent analysis is carried out by minimizing a global error function of the type shown in Eq. (2).

$$\begin{aligned}\sigma_i^2\left(n_i, k_i, \lambda_i, d_f, d_r\right) = \\ \left[T_i^{\mathrm{exp}} - T^{\mathrm{th}}\left(n_i, k_i, \lambda_i, d_f\right)\right]^2 + \\ \sum_j \left[S_{2,i}^{\mathrm{exp}} - S_2^{\mathrm{th}}\left(n_i, k_i, \lambda_i, \theta_j, d_f, d_r\right)\right]^2 + \\ \left[S_{3,i}^{\mathrm{exp}} - S_3^{\mathrm{th}}\left(n_i, k_i, \lambda_i, \theta_j, d_f, d_r\right)\right]^2\end{aligned} \tag{2}$$

Here, T is transmittance, θ_j is the incidence angle for the various ellipsometry measurements, and S_2 and S_3 are the second and third Stokes parameters, which are related to the usual ellipsometry measurements by Eq. (3), where p is the degree of polarization[13] The constants d_f and d_r are the film and rms roughness layer thicknesses, respectively.

$$\begin{cases} S_1 = -p\cos\left(2\psi\right) \\ S_2 = p\sin\left(2\psi\right)\cos\left(2\Delta\right) \\ S_3 = -p\sin\left(2\psi\right)\sin\left(2\Delta\right) \end{cases} \tag{3}$$

S_2 and S_3 are chosen over ψ and Δ as they tend to be better fitting variables. This is attributed to their typical value ranges being closer to each other and to those for T. Consequently, the minimization algorithm does not skew excessively towards one type of measurement. S_1 provides no additional information to the system, so it isn't necessary to include it in the error function. An example of a fit between the theoretical and experimental curves obtained using this procedure is shown in Fig. 1.

The effects of surface micro roughness are not considered for T. This is because, for low rms values, the resulting light scattering can be mostly compensated for by measuring total transmittance instead of only specular transmittance. Note that this is entirely equivalent to using the classical scalar scattering theory models for surface roughness, which assume the total transmittance of a rough sample to be equal to the specular transmittance of an equivalent flat sample.[14–17] On the other hand, it is necessary to consider surface roughness in ellipsometry (at least when probing on the film side, see section III C). This is done by the typical Bruggeman effective medium approximation (EMA), with a void fraction of 50%.[5–9,13]

As film and roughness layer thicknesses are not known beforehand, they are determined by minimizing the total error obtained from Eq. (2) for all wavelengths, as a function of d_f and d_r (see Eq. (4)).[5]

$$\sigma_{f,r}^2\left(d_f, d_r\right) = \sum_{i=1}^{N} \sigma_i^2\left(n_i, k_i, \lambda_i, d_f, d_r\right) \tag{4}$$

Here, N indicates the total number of measured wavelengths. In practice, the wavelengths used for this step should be limited to the region where T is noticeably greater than zero, to maximize accuracy. Further details on this procedure are outlined in a previous work.[5]

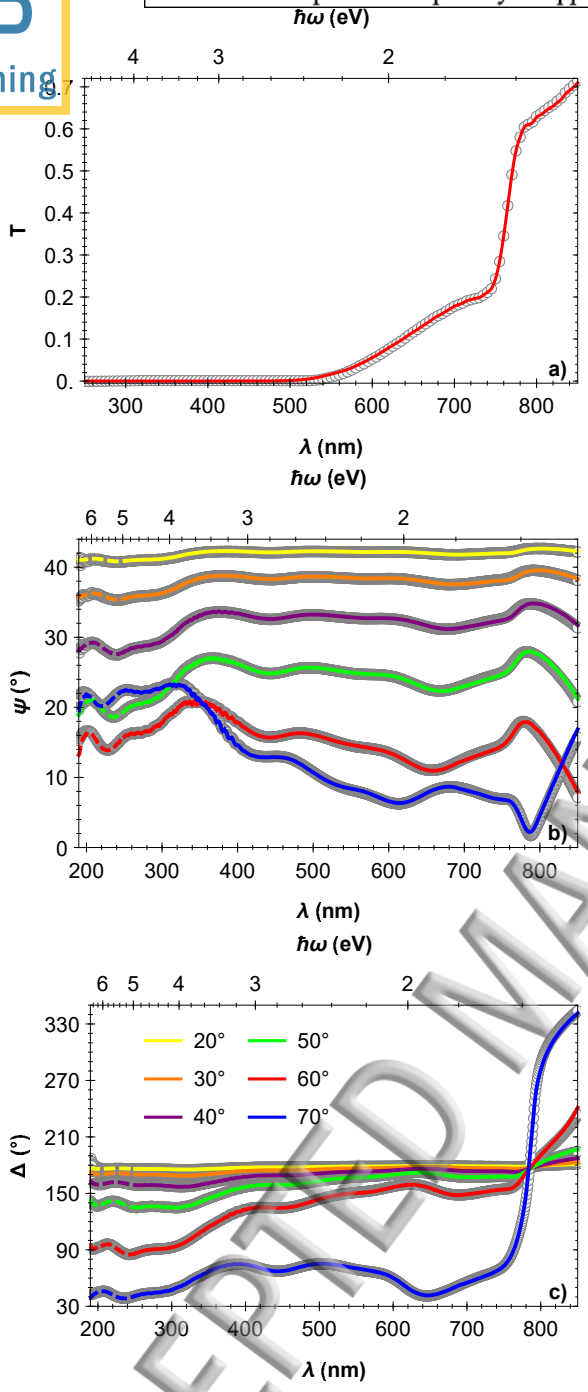

Figure 1. Transmittance T (a), and VASE variables ψ (b) and Δ (c) fit. Experimental curves (circles) and corresponding fits (solid curves) obtained with the self consistent approach. The example corresponds to a composition of $x = 0$. Solid curves correspond to the region where transmittance and ellipsometry spectra overlap (250 to 850 nm) whilst dashed lines correspond to theoretical curves calculated with ellipsometry data only (190 to 250 nm).

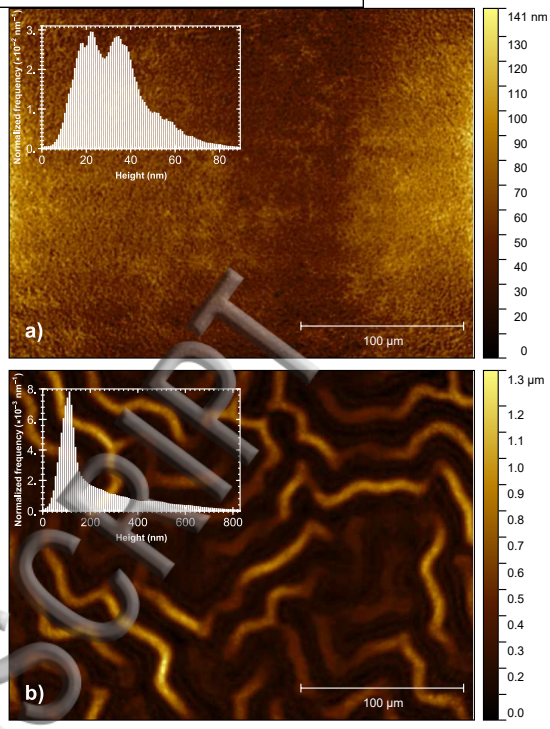

Figure 2. Laser confocal microscope images of typical flat (a) and wrinkle-textured (b) film topographies. They are the results of film manufacturing procedures **P1** and **P2**, respectively. Note the considerably different height scale of the color maps. Insets are normalized histograms displaying the height distributions of each image.

C. Film topography considerations

Two types of films were studied: one with a generally flat, though still somewhat inhomogeneous topography (Procedure 1, **P1**), and one with a strongly wrinkled self-texturing effect caused by the deposition parameters (Procedure 2, **P2**). Examples of both are shown in Fig. 2. In order to obtain accurate estimates for n and k, the effects of these topographies on the optical measurements had to be considered. To this end, surface topography images for each sample were recorded with a laser confocal microscope. The images were leveled by mean plane subtraction and smoothed with a Gaussian filter to remove high frequency noise and anomalous peaks.

To include the topography effects in the optical models, the height data in the images was then used to build a histogram (see Fig. 2 insets), from which a normalized probability distribution function f for the film height was calculated. This could then be used to average the transmittance and ellipsometry variables, as seen in Eqs. (5) and (6), respectively.[13,18,19]

$$\langle T \rangle = \int T(d+t) f(t)\, dt \tag{5}$$

$$\langle S_n \rangle = \int S_n(d+t) f(t)\, dt \quad (n = 1, 2, 3) \tag{6}$$

Here, t is the height of a thickness variation layer on top of a layer with constant thickness d (recalling section III B, the roughness layer would be on top of the t layer). Note that this is completely equivalent to averaging over the imaging area, as seen in Eq. (7), where $\mathcal{A}$ is the imaged area.[16] The main advantage of averaging over height frequency is increased calculation speed, as the

integrals in Eqs. (5) and (6) are one-dimensional and require far fewer computations of $T(d+t)$ and $S_n(d+t)$ for the same level of precision.

$$\langle T \rangle = \iint_{\mathcal{A}} T\left(d + t\left(x, y\right)\right) dxdy \tag{7}$$

The models for T and S_n to be averaged are standard ones obtained through Fresnel coefficient addition for the corresponding sample and probing beam configurations.[13,16] The refractive index for the fused quartz substrate is modeled with a Sellmeier series, previously fitted to measurements of the substrate only. The effect of internal reflections in the substrate is also considered.

With these considerations and those of section III B in mind, the complex refractive index for the various flat topography films are shown in Fig. 3. These samples are analyzed with the ellipsometry probing beam incident on the film side.

The wrinkle-textured films require some additional considerations. Due to their optically diffuse nature, the ellipsometer was often unable to collect enough light for proper measurements. To get around this problem, these samples were measured with the probing beam incident on the substrate side of the sample, which required the use of a depolarizing model that considers the incoherent light passing through the quartz glass.[13] Because of this, the degree of polarization p was also measured to be used in Eq. (3) ($p \approx 1$ for the flat samples).

It was observed in practice that using a simplified ellipsometry model, assuming the film to be an infinite homogeneous medium beneath the quartz substrate, was just as effective as the fully detailed model. This is attributed to the large thickness of these films ($\sim 1\,\mu$m), the scattering effect of the wrinkled texturing and the intermediate reflections in the substrate, which results in practically no light reflected from the bottom layer of the sample reaching the detector. This assumption breaks down slightly as absorption approaches zero, but is compensated for by the transmittance measurements, for which the complete optical model is considered. While this may seem inconsequential, it allowed the film thickness to be calculated much quicker, as Eq. (4) would then only depend on d_f. With these considerations in mind, the complex refractive index for the various wrinkle-textured films are shown in Fig. 4.

There are some slight differences between the $n(\lambda)$ and $k(\lambda)$ curves shown in Figs. 3 and 4, particularly in higher energy regions. Even though the compositions for both the flat and wrinkle-textured films are the same, they were formed under different deposition conditions. This could have yielded somewhat differing levels of atomic disorder and therefore internal stresses within the bulk material, which can distort the band structure and therefore $\tilde{n}(\lambda)$ as well. Differences in the deep UV may be partly due to the quartz substrate becoming slightly absorbing near 190 nm, as well as information loss due to the depolarizing nature of the measurements for the wrinkle-textured films.

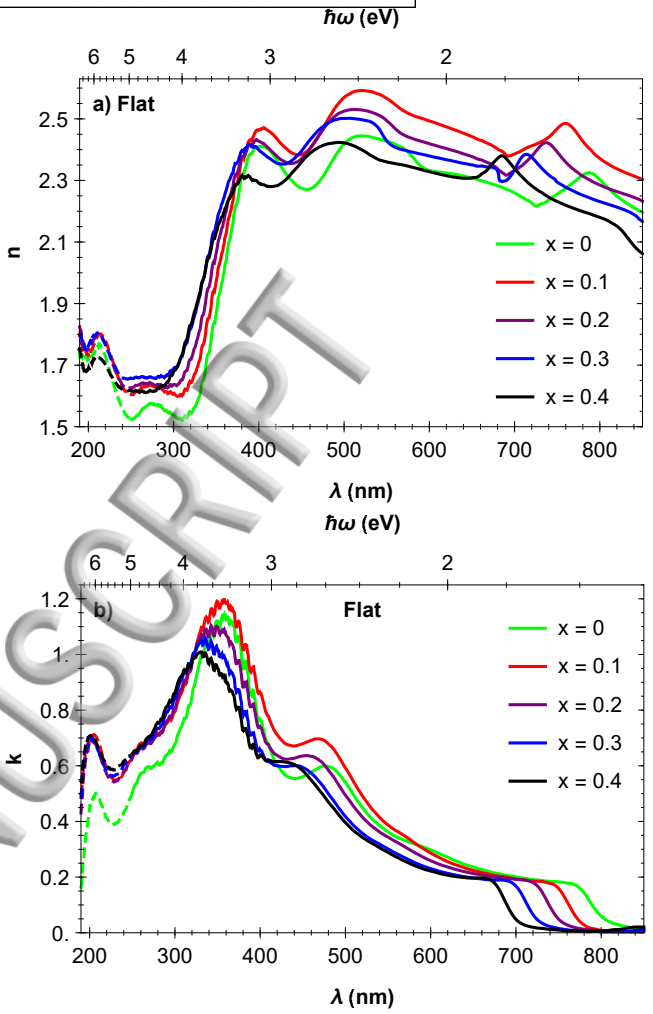

Figure 3. Refractive indices (a) and extinction coefficients (b) of the flat topography perovskite films for various stoichiometries. Here, x corresponds to $FA_{0.83}Cs_{0.17}Pb(I_xBr_{1-x})_3$. Solid lines correspond to calculations obtained from both T and ellipsometry (250 to 850 nm), and dashed lines correspond to the calculation performed with ellipsometry only (190 to 250 nm).

IV. BANDGAP CALCULATION

The optical bandgap E_g is calculated from the absorption coefficient α, which is obtained from the previously calculated k values by $\alpha = 4\pi k/\lambda$. The classical procedure for achieving this, which uses a fundamental absorption model for optical band-to-band transitions in direct bandgap materials, involves fitting a linear region located near the absorption edge in a $(\alpha \cdot \hbar\omega)^2$-plot.[20] This can also be done using quantum efficiency measurements in a similar fashion.[21] While this is a very simple and straightforward approach, the linear region in question is arbitrarily delimited, and partial overlap with the Urbach tail may result in few available measurement points as well as a systematic bias in the yielded bandgap values.[5,22] These issues, which can limit the accuracy and reliability of the procedure, can be compensated for by instead using a model that considers a larger spectral region. For this purpose, a band fluctuations model for direct semicon-

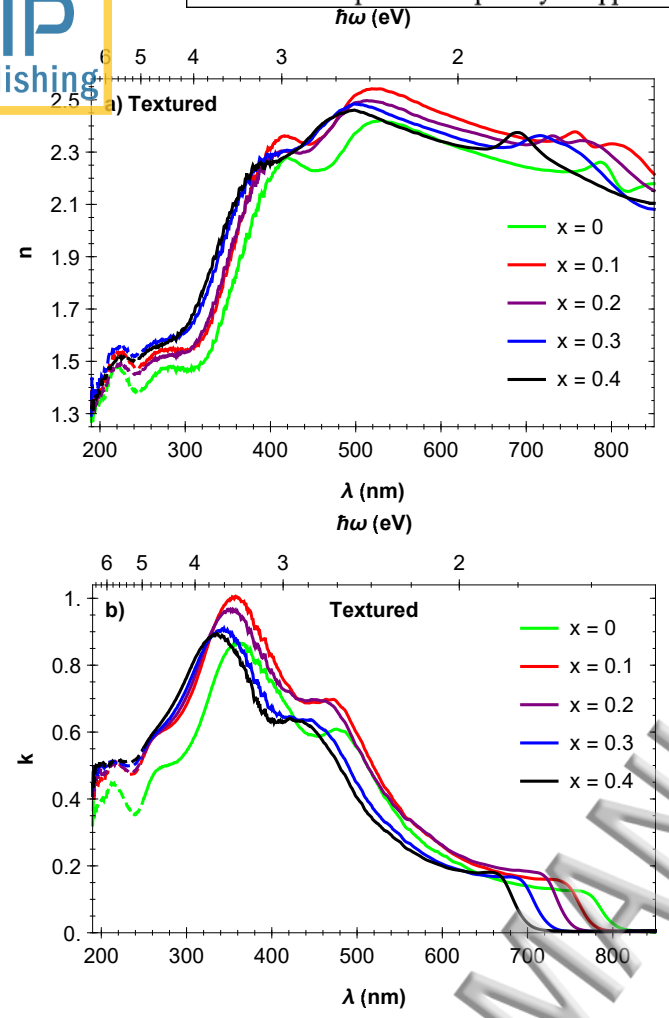

Figure 4. Refractive indices (a) and extinction coefficients (b) of the wrinkle-textured perovskite films for various stoichiometries. Here, x corresponds to $FA_{0.83}Cs_{0.17}Pb(I_xBr_{1-x})_3$. Solid and dashed lines have the same meaning as in Fig. 3.

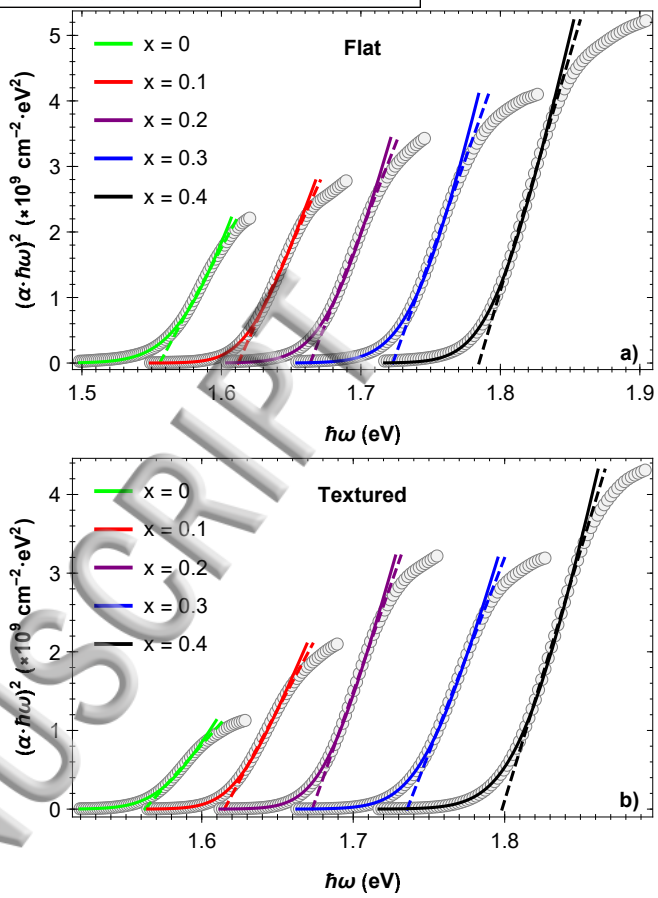

Figure 5. Fitted absorption coefficients shown in $(\alpha \cdot \hbar\omega)^2$-plots for the flat topography films (a) and the wrinkle-textured films (b). Circles correspond to the absorption coefficients obtained from the k values in Figs. 3 and 4. Solid lines correspond to fits with the band fluctuations model whilst dashed lines to linear fits with the direct bandgap model.

ductors developed in a previous work,[5] which describes both the Urbach tail and fundamental absorption region in a single equation, is chosen (see Eq. (8)).

$$\alpha(\hbar\omega) = -\frac{1}{2}\frac{\alpha_0}{\hbar\omega}\sqrt{\frac{\pi}{\beta}}\mathrm{Li}_{1/2}\left(-e^{\beta(\hbar\omega - E_g)}\right) \qquad (8)$$

Here, $\mathrm{Li}_n(x)$ is the n-th order polylogarithm function of x, α_0 is a constant and $\beta = 1/E_U$, with E_U the Urbach energy. A comparison between fits achieved with this model and the direct bandgap model for all the samples in this work is shown in Fig. 5.

From the fits in Fig. 5, the values for E_g and E_U can be extracted; they are shown in Fig. 6. Typical error values for both E_g and E_U are ± 0.001 eV. Very good correspondence between the bandgap values for the flat and wrinkled films is observed, as well as between the band fluctuations and conventional models. A slight offset can be seen between the values obtained with either model, which is attributed to the limitations of the conventional strategy, outlined previously. The Urbach energies on the other hand, while generally increasing with Br concentration in both cases, are systematically different for the two film morphologies. As the Urbach energy is indicative of lattice disorder,[22,23] the generally lower values found for the wrinkle-textured films can be attributed to the different deposition parameters. In particular, the textured samples had a two-stage annealing process with increasing temperatures (instead of a single stage process for the flat samples), which may have resulted in larger grain sizes. This can also partially account for the slight differences in the complex refractive indices, shown in Figs. 3 and 4 (see section III C).

Within the considered stoichiometries, the bandgap increases quite linearly from 1.564 eV to 1.792 eV, with a slope parameter dE_g/dx of 0.575 eV (values averaged between flat and wrinkle-textured films), which is consistent with Vegard's law.[1] Thus the material's optical bandgap is not only highly tunable,[1,10] but is so in a predictable way within the range of $x = 0$ to 0.4. Finally, it is possible to interpolate the composition that would yield the ideal 1.75 eV[1–3,12] bandgap necessary for a Si-perovskite tandem solar cell. This is determined to be $x = 0.33$, or $FA_{0.83}Cs_{0.17}Pb(I_{0.67}Br_{0.33})_3$.

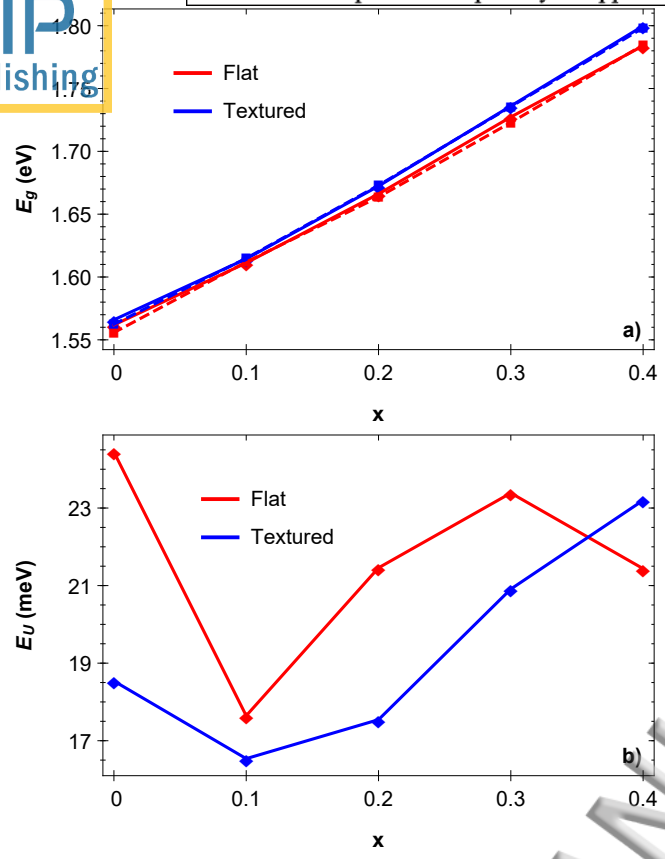

Figure 6. Optical bandgap E_g (a) and Urbach energy E_U (b) obtained for the various perovskite stoichiometries. Solid lines and diamond markers correspond to fits with the band fluctuations model, whilst dashed lines and square markers correspond to fits with the fundamental absorption model.

V. SUMMARY

To summarize, the complex refractive index for both flat and textured topography $FA_{0.83}Cs_{0.17}Pb(I_{1-x}Br_x)_3$ perovskite films of various compositions was determined (see Figs. 3 and 4). This was achieved using a combination of transmittance and ellipsometry at various angles via a self consistent point-by-point approach using suitable optical models which included film thickness variation, surface roughness and internal reflections in the substrate for maximal accuracy. The optical bandgap and Urbach energy were then calculated using a band fluctuations model for direct semiconductors, and compared with a conventional fundamental band-to-band absorption model (see Figs. 5 and 6). In both cases, results show that the bandgap can predictably be tuned within a considerable range (at least from 1.564 eV to 1.792 eV). Finally, the composition that would yield the ideal 1.75 eV bandgap for a Si-perovskite tandem solar cell is inferred to be $FA_{0.83}Cs_{0.17}Pb(I_{0.67}Br_{0.33})_3$.

ACKNOWLEDGMENTS

This work was funded by the Research Management Office of the Pontificia Universidad Católica del Perú (PUCP), project 2017-1-0030/502. Additional support has been provided by the German Academic Exchange Service (DAAD) in conjunction with the Peruvian National Fund for Scientific and Technological Development (FONDECYT) (grants no. 037-2016 and no. 132-2017), the Research Internationalization Office of the PUCP, the German Federal Ministry of Education and Research (BMBF), within the project "Materialforschung für die Energiewende" (grant no. 03SF0540), and the German Federal Ministry for Economic Affairs and Energy (BMWi) through the "PersiST" project (grant no. 0324037C). A.T. gratefully acknowledges Cienciactiva CONCYTEC for a MSc scholarship. S.B. gratefully acknowledges the Alexander von Humboldt Foundation for a Feodor Lynen Research Fellowship.

REFERENCES

[1] D. P. McMeekin, G. Sadoughi, W. Rehman, G. E. Eperon, M. Saliba, M. T. Horantner, A. Haghighirad, N. Sakai, L. Korte, B. Rech, M. B. Johnston, L. M. Herz, and H. J. Snaith, Science **351**, 151 (2016).
[2] M. Anaya, G. Lozano, M. E. Calvo, and H. Míguez, Joule **1**, 769 (2017).
[3] K. A. Bush, A. F. Palmstrom, Z. J. Yu, M. Boccard, R. Cheacharoen, J. P. Mailoa, D. P. McMeekin, R. L. Z. Hoye, C. D. Bailie, T. Leijtens, I. M. Peters, M. C. Minichetti, N. Rolston, R. Prasanna, S. Sofia, D. Harwood, W. Ma, F. Moghadam, H. J. Snaith, T. Buonassisi, Z. C. Holman, S. F. Bent, and M. D. McGehee, Nature Energy **2**, 17009 (2017).
[4] M. S. Alias, I. Dursun, M. I. Saidaminov, E. M. Diallo, P. Mishra, T. K. Ng, O. M. Bakr, and B. S. Ooi, Optics Express **24**, 16586 (2016).
[5] J. A. Guerra, A. Tejada, L. Korte, L. Kegelmann, J. A. Töfflinger, S. Albrecht, B. Rech, and R. Weingärtner, Journal of Applied Physics **121**, 173104 (2017).
[6] P. Löper, M. Stuckelberger, B. Niesen, J. Werner, M. Filipič, S.-J. Moon, J.-H. Yum, M. Topič, S. De Wolf, and C. Ballif, The Journal of Physical Chemistry Letters **6**, 66 (2015).
[7] P. F. Ndione, Z. Li, and K. Zhu, J. Mater. Chem. C **4**, 7775 (2016).
[8] M. Shirayama, H. Kadowaki, T. Miyadera, T. Sugita, M. Tamakoshi, M. Kato, T. Fujiseki, D. Murata, S. Hara, T. N. Murakami, S. Fujimoto, M. Chikamatsu, and H. Fujiwara, Physical Review Applied **5**, 014012 (2016).
[9] M. Kato, T. Fujiseki, T. Miyadera, T. Sugita, S. Fujimoto, M. Tamakoshi, M. Chikamatsu, and H. Fujiwara, Journal of Applied Physics **121**, 115501 (2017).
[10] C. Yi, J. Luo, S. Meloni, A. Boziki, N. Ashari-Astani, C. Grätzel, S. M. Zakeeruddin, U. Röthlisberger, and M. Grätzel, Energy & Environmental Science **9**, 656 (2016).
[11] NREL, "https://www.nrel.gov/pv/assets/images/efficiency-chart.png," (2018).
[12] S. P. Bremner, M. Y. Levy, and C. B. Honsberg, Progress in Photovoltaics: Research and Applications **16**, 225 (2008).
[13] H. Fujiwara, *Spectroscopic Ellipsometry* (John Wiley & Sons, Ltd, Chichester, UK, 2007).
[14] G. Yin, C. Merschjann, and M. Schmid, Journal of Applied Physics **113**, 213510 (2013).
[15] M. Zeman, R. A. C. M. M. van Swaaij, J. W. Metselaar, and R. E. I. Schropp, Journal of Applied Physics **88**, 6436 (2000).
[16] J. Szczyrbowski, Journal of Physics D: Applied Physics **11**, 021 (1978).
[17] C. K. Carniglia, Optical Engineering **18**, 104 (1979).
[18] P. I. Rovira and R. W. Collins, Journal of Applied Physics **85**, 2015 (1999).
[19] C.-C. Lin, W.-L. Liu, and C.-Y. Hsieh, Journal of Applied Physics **109**, 014508 (2011).

[20]P. Y. Yu and M. Cardona, *Fundamentals of Semiconductors*, Graduate Texts in Physics (Springer Berlin Heidelberg, Berlin, Heidelberg, 2010).
[21]M. Samiee, S. Konduri, B. Ganapathy, R. Kottokkaran, H. A. Abbas, A. Kitahara, P. Joshi, L. Zhang, M. Noack, and V. Dalal, Applied Physics Letters **105**, 3 (2014).
[22]J. A. Guerra, J. R. Angulo, S. Gomez, J. Llamoza, L. M. Montañez, A. Tejada, J. A. Töfflinger, A. Winnacker, and R. Weingärtner, Journal of Physics D: Applied Physics **49**, 195102 (2016).
[23]R. A. Street, *Hydrogenated amorphous silicon* (Cambridge University Press, Cambridge, 1991).

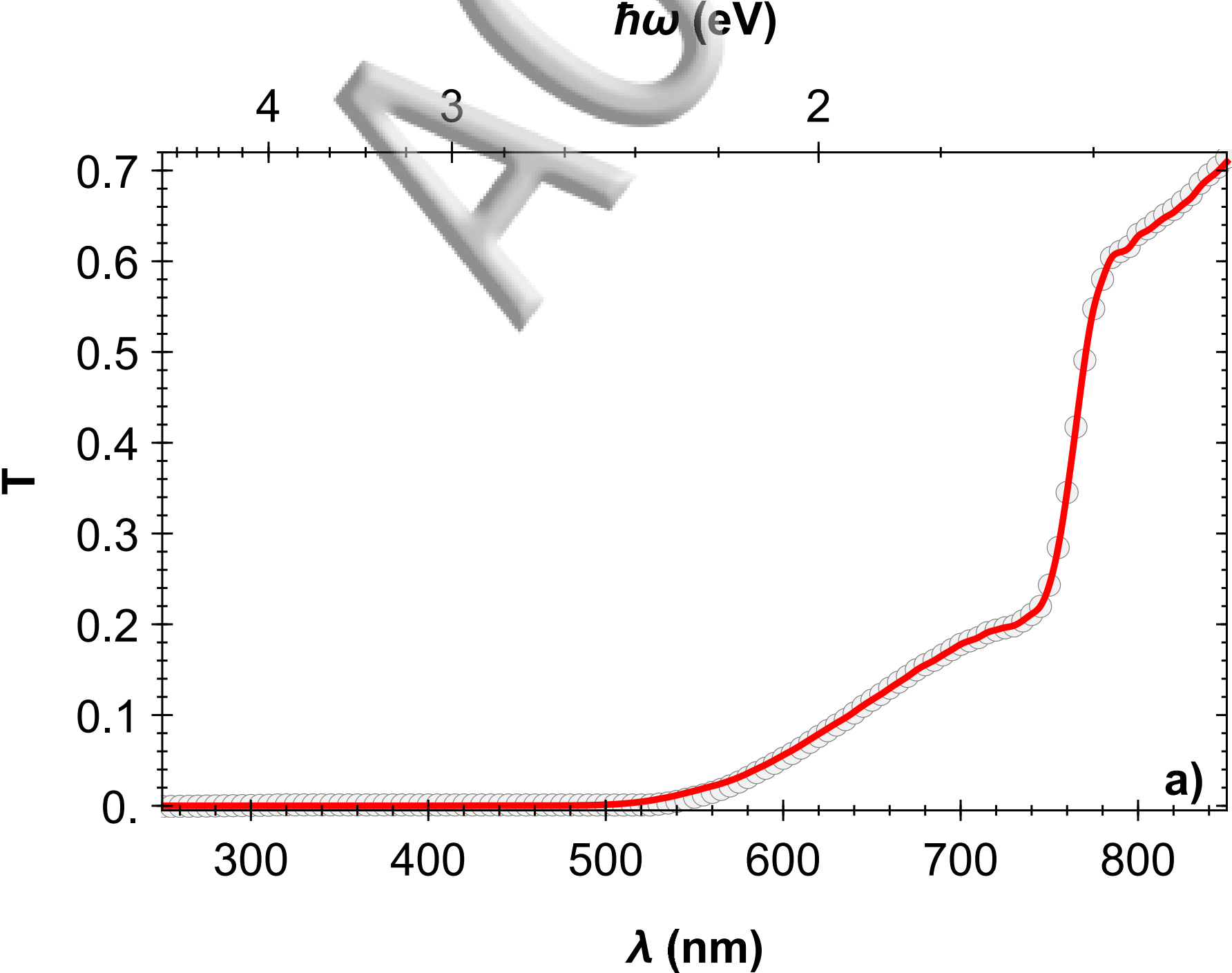
ħω (eV)
4
3
2
0.7
0.6
0.5
0.4
0.3
0.2
0.1
0.
T
a)
300
400
500
600
700
800
λ (nm)

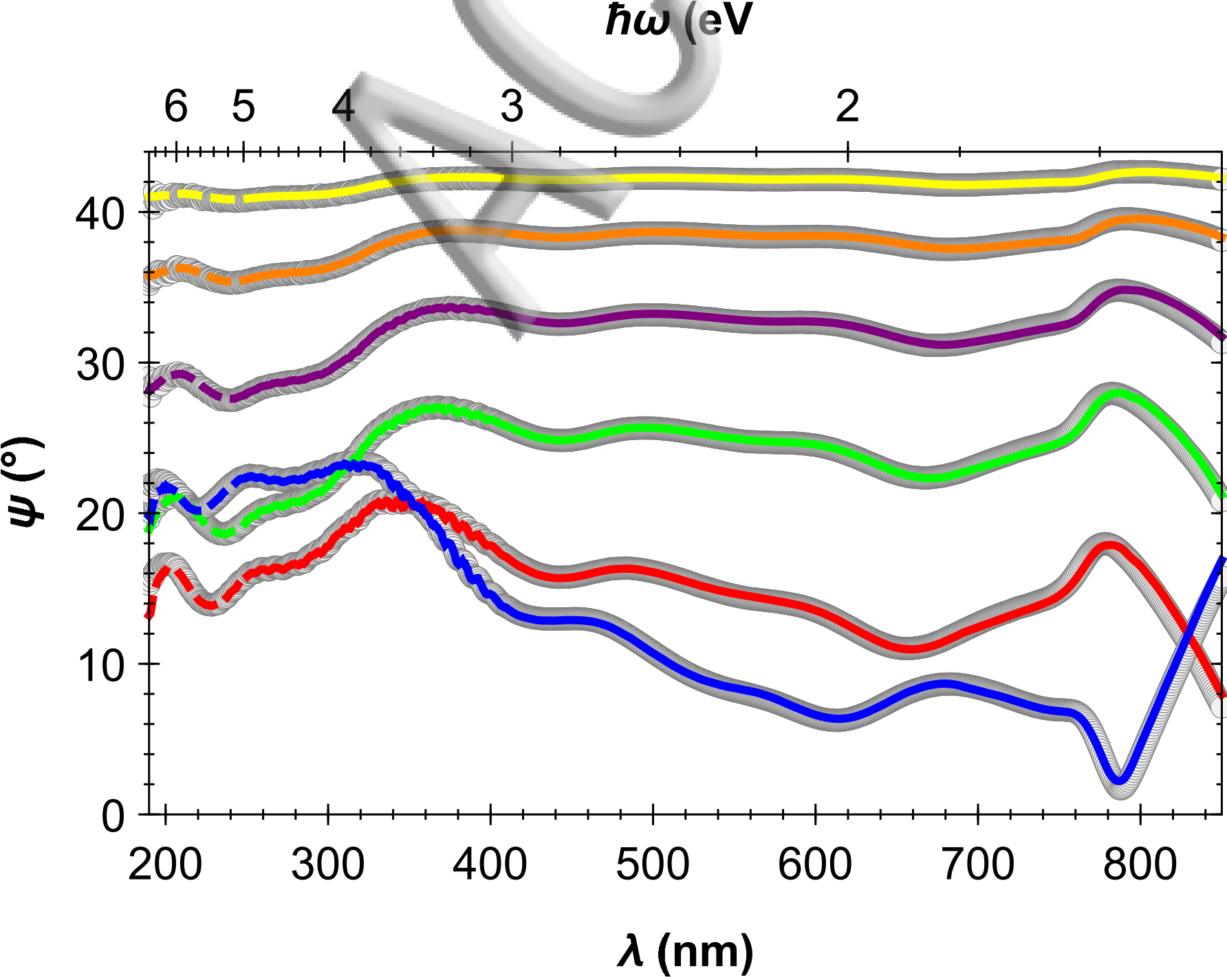
ħω (eV
6
5
4
3
2
40
30
20
10
0
ψ (°)
200
300
400
500
600
700
800
λ (nm)

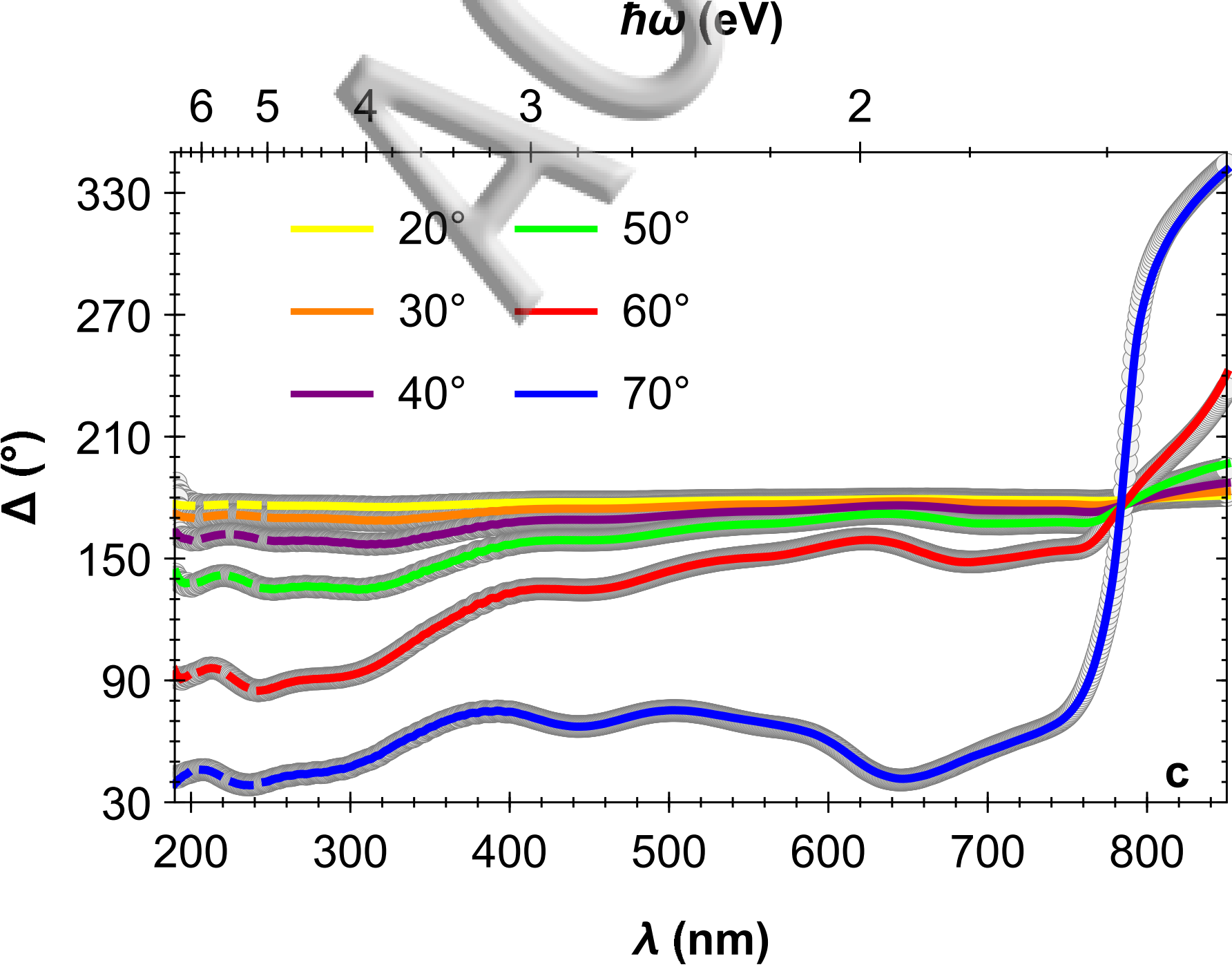
ħω (eV)
6
5
4
3
2
330
270
210
150
90
30
Δ (°)
20°
30°
40°
50°
60°
70°
c
200
300
400
500
600
700
800
λ (nm)

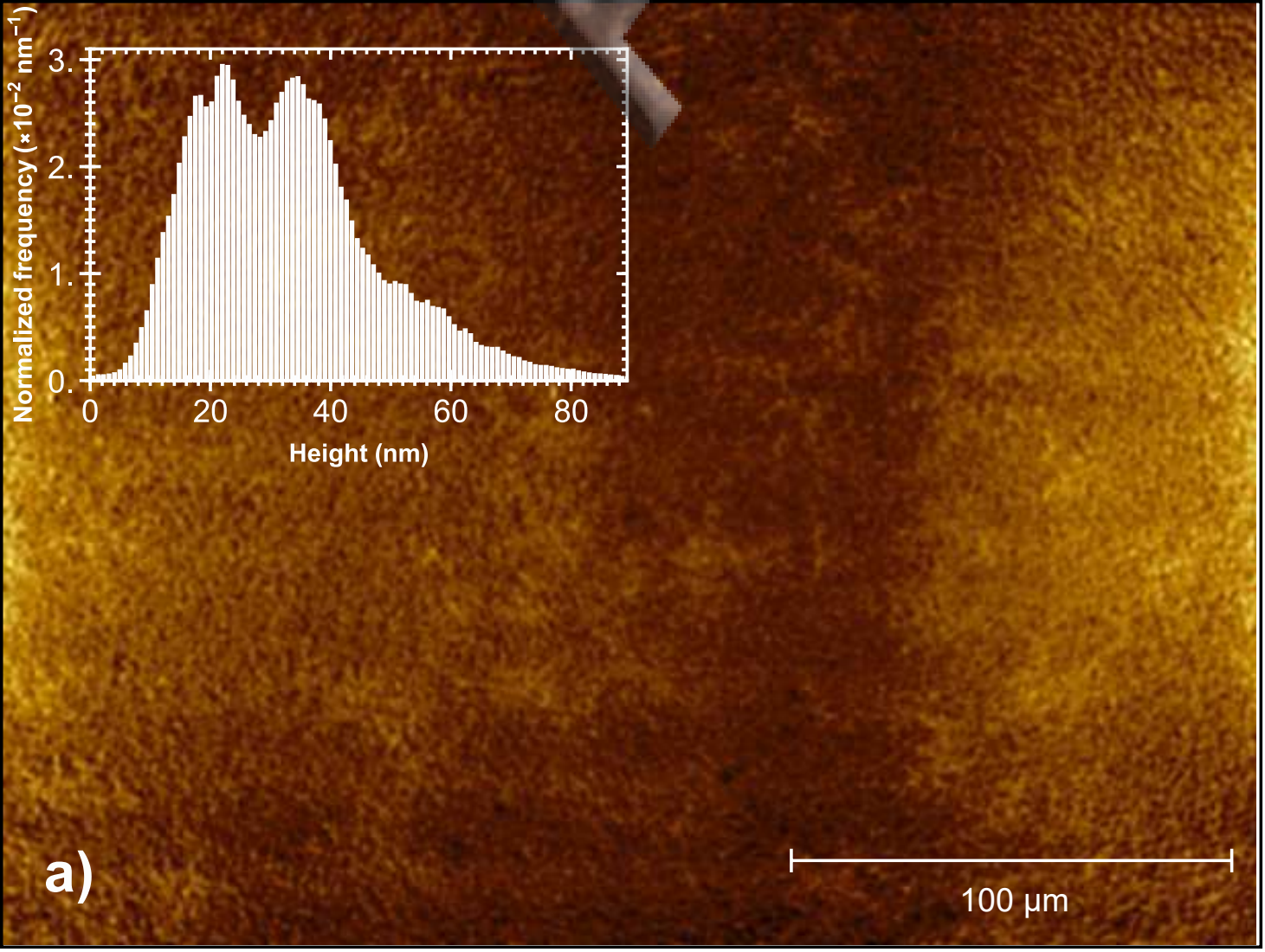
Normalized frequency (×10^{-2} nm^{-1})
3.
2.
1.
0.
0
20
40
60
80
Height (nm)
a)
100 µm
141 nm
130
120
110
100
90
80
70
60
50
40
30
20
0

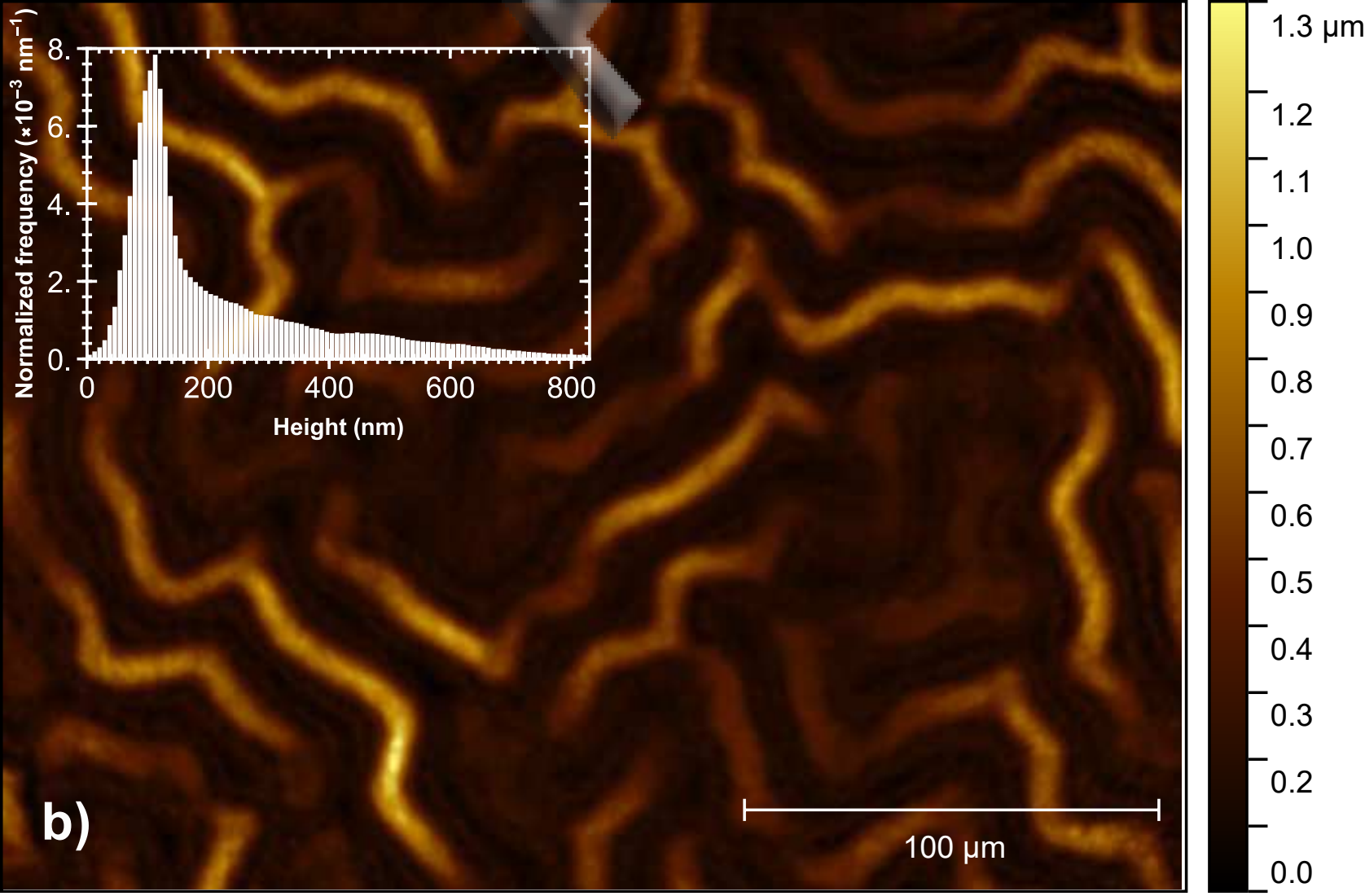
Normalized frequency (×10⁻³ nm⁻¹)
8.
6.
4.
2.
0.
0
200
400
600
800
Height (nm)
b)
100 µm
1.3 µm
1.2
1.1
1.0
0.9
0.8
0.7
0.6
0.5
0.4
0.3
0.2
0.0

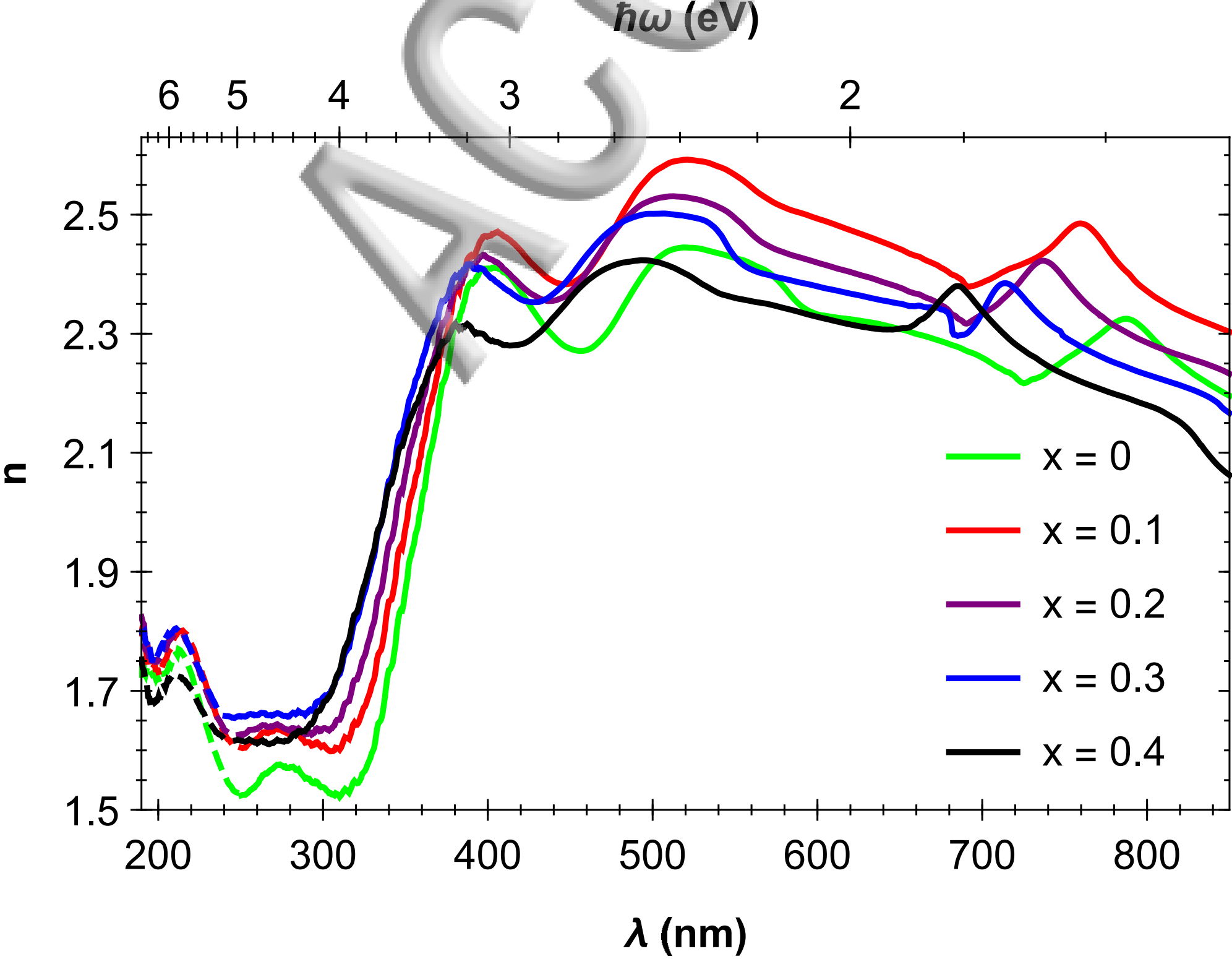
ħω (eV)
6
5
4
3
2
2.5
2.3
2.1
1.9
1.7
1.5
n
200
300
400
500
600
700
800
λ (nm)
x = 0
x = 0.1
x = 0.2
x = 0.3
x = 0.4

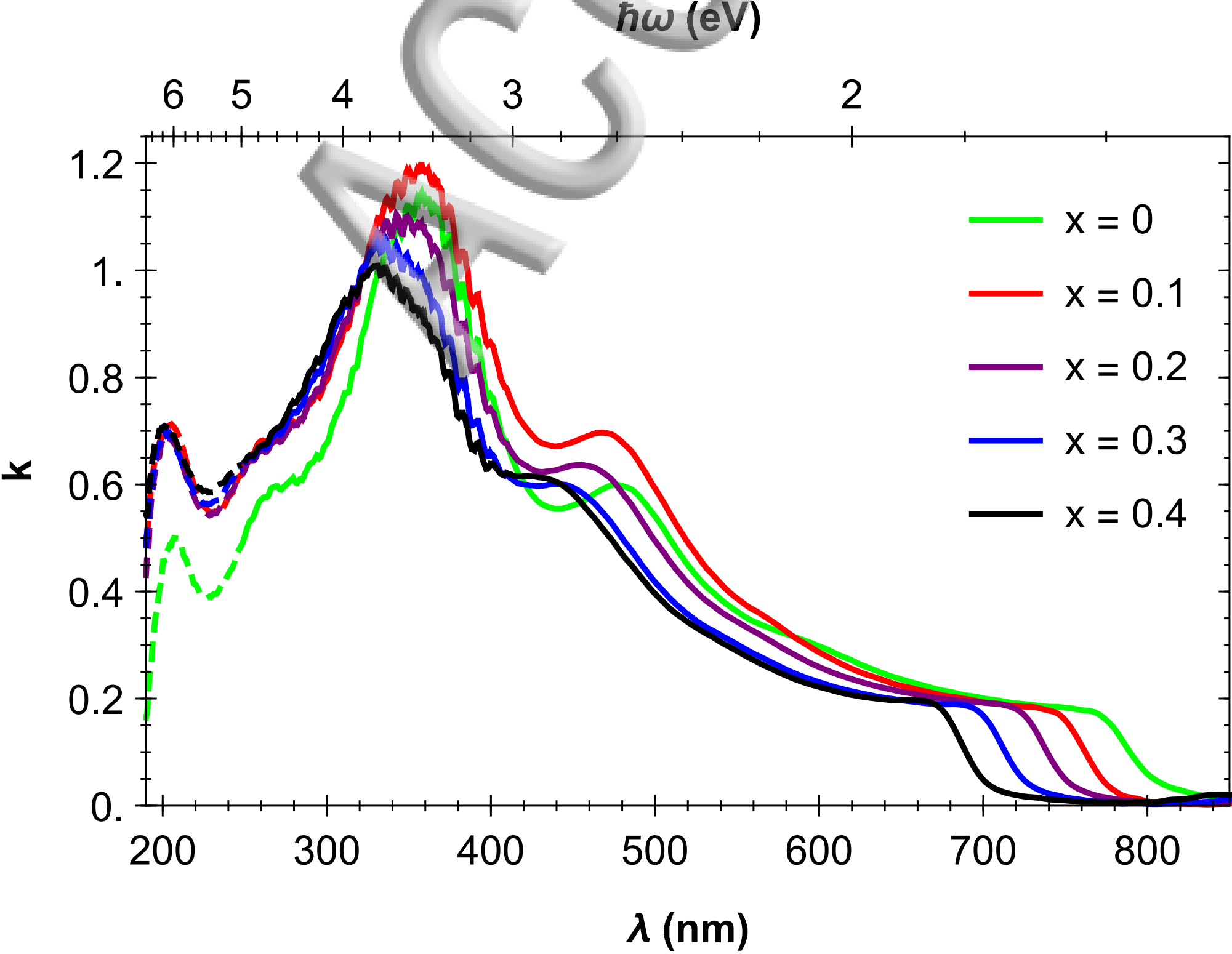
ħω (eV)
6
5
4
3
2
1.2
1.
0.8
0.6
0.4
0.2
0.
k
200
300
400
500
600
700
800
λ (nm)
x = 0
x = 0.1
x = 0.2
x = 0.3
x = 0.4

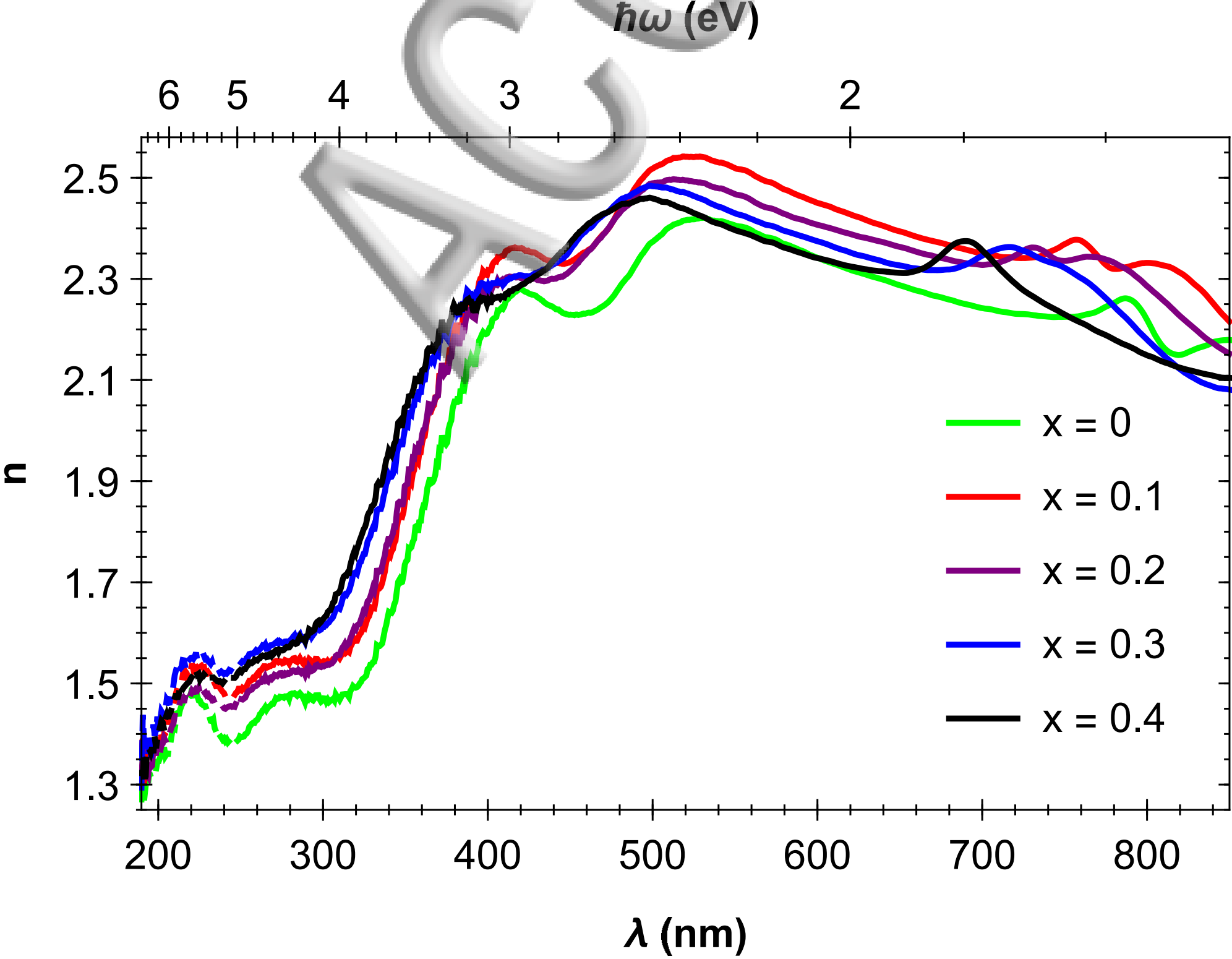
ħω (eV)
6
5
4
3
2
2.5
2.3
2.1
1.9
1.7
1.5
1.3
n
200
300
400
500
600
700
800
λ (nm)
x = 0
x = 0.1
x = 0.2
x = 0.3
x = 0.4

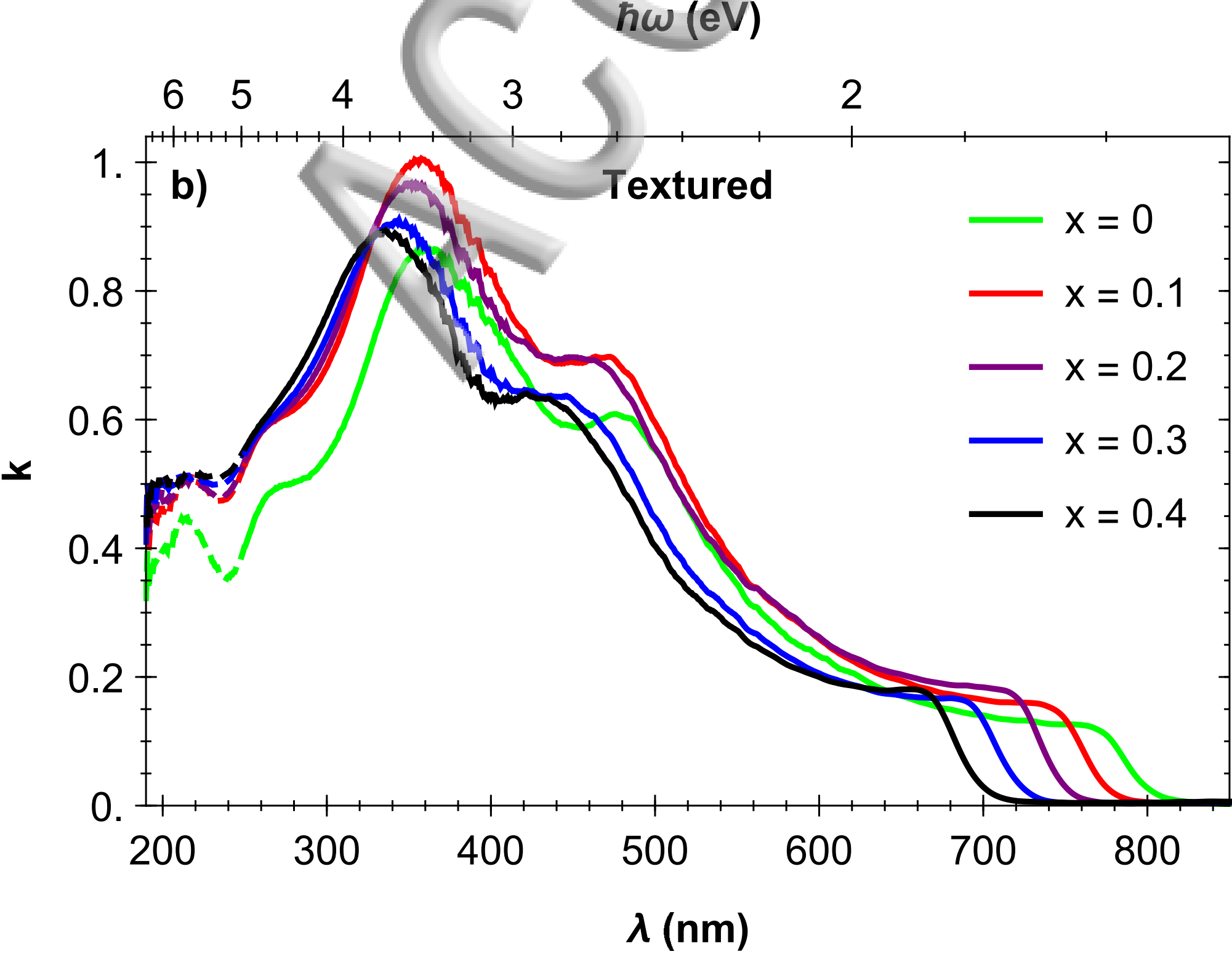
ħω (eV)
6
5
4
3
2
b)
Textured
x = 0
x = 0.1
x = 0.2
x = 0.3
x = 0.4
k
1.
0.8
0.6
0.4
0.2
0.
200
300
400
500
600
700
800
λ (nm)

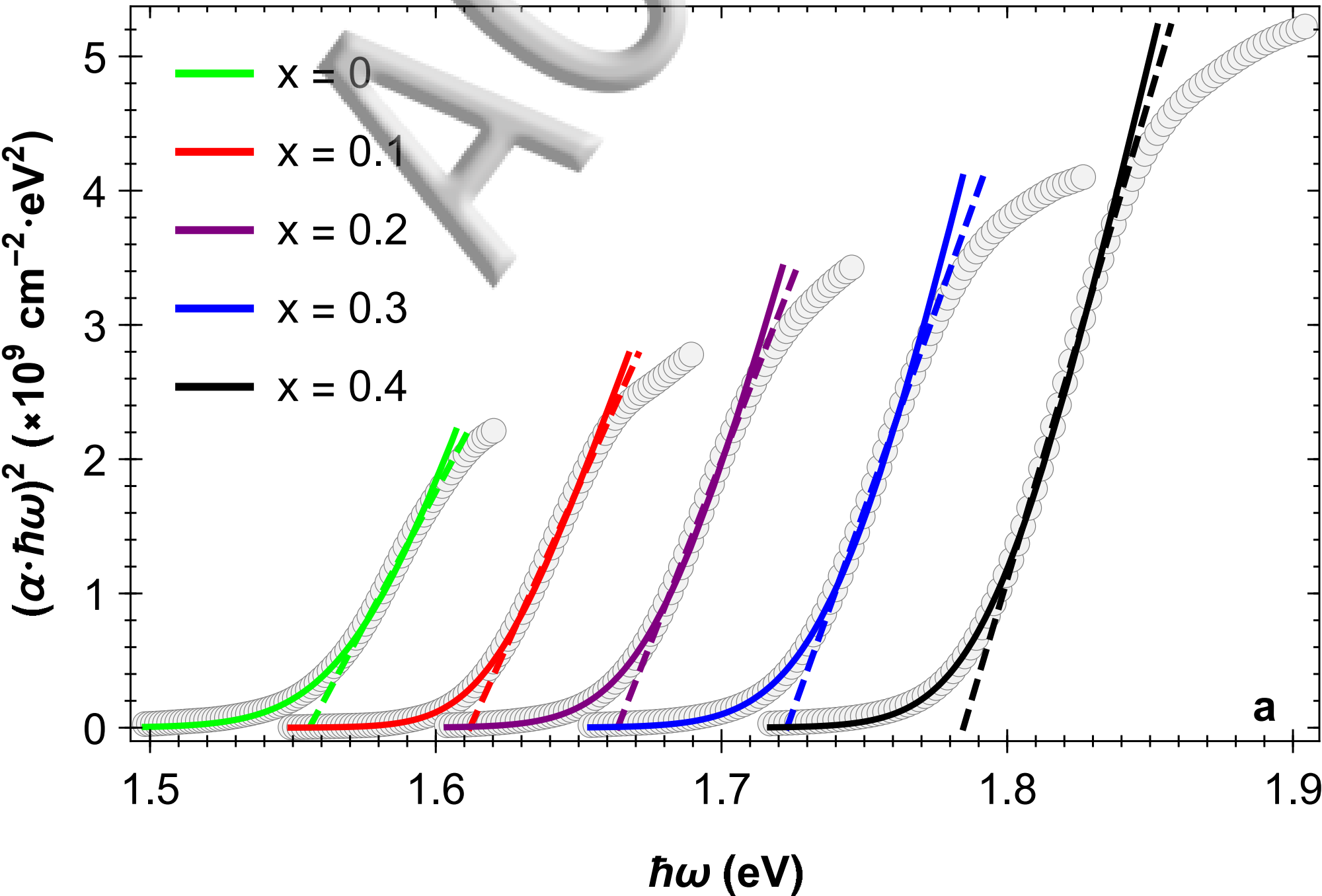
x = 0
x = 0.1
x = 0.2
x = 0.3
x = 0.4
$(\alpha \cdot \hbar\omega)^2$ ($\times 10^9$ cm^{-2}·eV^2)
$\hbar\omega$ (eV)
a
0
1
2
3
4
5
1.5
1.6
1.7
1.8
1.9

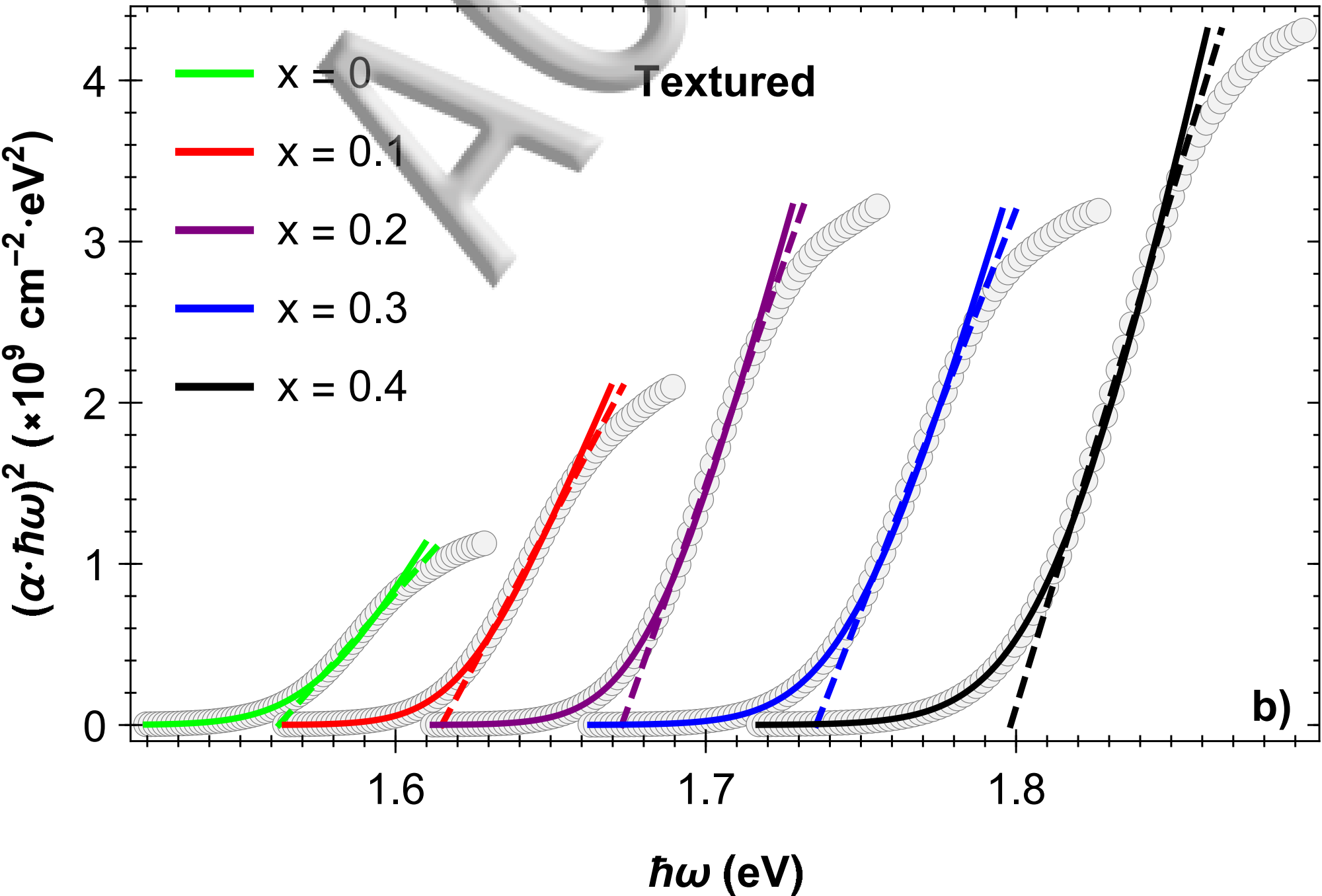
x = 0
x = 0.1
x = 0.2
x = 0.3
x = 0.4
Textured
b)
$(\alpha \cdot \hbar\omega)^2$ ($\times 10^9$ cm^{-2}·eV^2)
$\hbar\omega$ (eV)
0
1
2
3
4
1.6
1.7
1.8

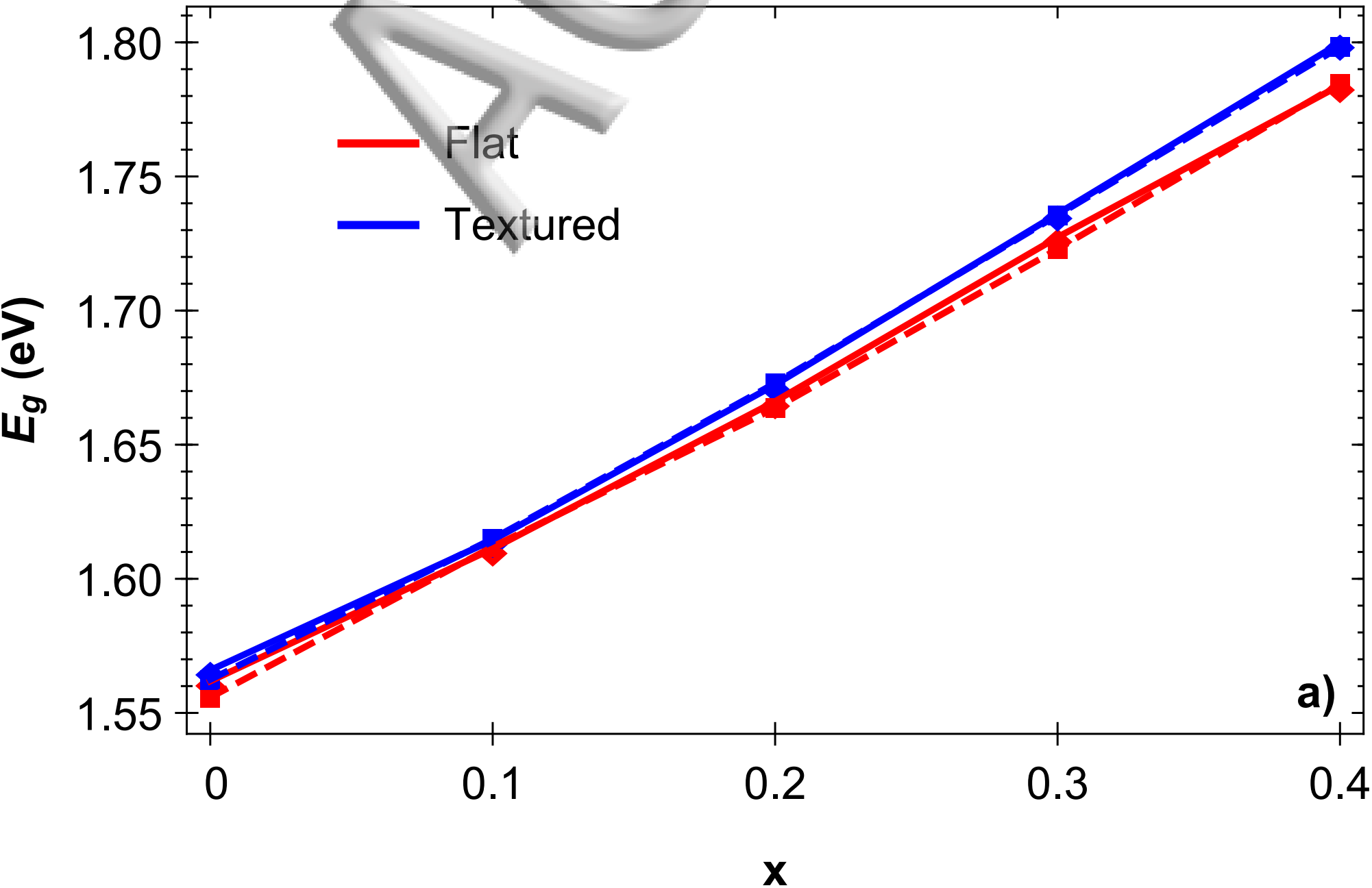
Flat
Textured
E_g (eV)
1.80
1.75
1.70
1.65
1.60
1.55
0
0.1
0.2
0.3
0.4
x
a)

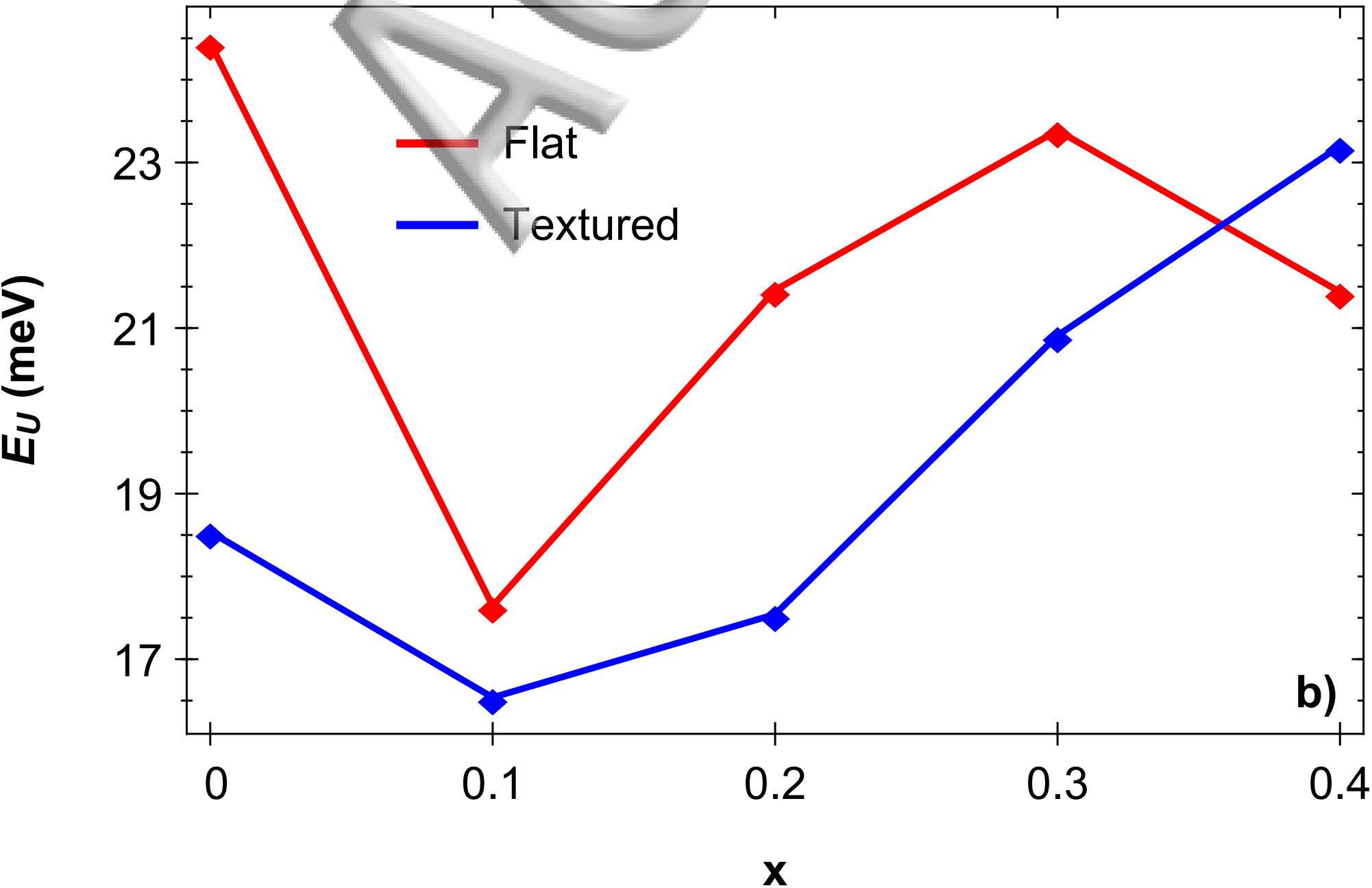
Flat
Textured
23
21
19
17
E_U (meV)
0
0.1
0.2
0.3
0.4
x
b)